

Computation of wave effects using the panel method

C.-H. Lee¹ & J. N. Newman^{1,2}

¹*WAMIT Inc., USA (www.wamit.com)*

²*Department of Ocean Engineering, MIT, USA*

1 Introduction

Numerical techniques for the prediction of wave effects have achieved an important role in offshore engineering, comparable to physical experiments. For large structures it is appropriate in most cases to use the linear (or weakly nonlinear) potential theory. This permits us to consider structures of quite general geometrical form, for a broad variety of applications. We restrict our attention here to fixed structures and vessels which are free to move in small unsteady motions. Thus we exclude the seakeeping problem for ships which are underway with substantial forward velocity.

The panel method, also known as the boundary integral equation method (BIEM), has been widely used for this purpose. The fundamental basis for this method is a form of Green's theorem where the velocity potential at any point in the fluid is represented by surface distributions of singularities over the boundary surfaces [1, 2, 3, 4]. Generally this leads to an integral equation which must be solved for the unknown source strength or dipole moment. This procedure was mainly of theoretical interest until Hess and Smith [5] developed the panel method and demonstrated its validity for three-dimensional bodies in unbounded fluid domains.

The method of Hess and Smith is referred to as the 'low-order panel method', to distinguish it from various higher-order extensions. The essential steps in the low-order method can be enumerated as follows: (1) the potential is represented either by a source distribution of unknown strength

over the body surface (the ‘source formulation’), or by Green’s theorem where the source strength is known and the dipole moment is equal to the unknown potential (the ‘potential formulation’); (2) the body surface is approximated by a large number N of small quadrilateral panels; (3) the source strength and dipole moment are assumed constant on each panel, giving a total of N unknowns; (4) in the source formulation the normal derivative of the potential is evaluated at the centroid of each panel, and set equal to the normal velocity at that point (in the potential formulation the potential itself is evaluated directly at the same points) giving a total of N linear equations for the unknown source strengths (or potentials); (5) this system of equations is solved by standard methods of linear algebra; (6) from this potential the pressure on each panel is evaluated, and integrated to compute the required forces and moments. This method has been applied in various fields of applied mechanics, particularly in aerodynamics [6].

Substantial efforts have been made to apply the same method to free-surface problems involving floating or submerged bodies. The first free-surface panel methods were hampered by the limitations of digital computers, and also by the complexity of the free-surface Green function (i.e. source potential). Nevertheless, important engineering analyses were performed with crude representations of the geometry based on discretizations with a few hundred panels, and often at considerable expense in terms of the computing time. These difficulties have essentially vanished, due to parallel improvements in the computers themselves (hardware) and the numerical techniques (software).

Accurate numerical approximations of the free-surface Green function were developed by Newman [7, 8] which are valid for all ranges of the frequency and water depth. Based on this development, and with the use of an iterative method of solution of the linear system developed by Lee [9], Korsmeyer *et al* [10] analyzed complex offshore structures such as a tension leg platform (TLP) using up to 12000 panels to demonstrate the convergence of the linear solutions.

With the facility to perform robust computations of the linearized (first-order) potential, and with the growing importance of the TLP, efforts were devoted to the development of programs capable of solving for the second-order potential. (Here ‘second-order’ refers to the inclusion of quadratic terms in the weakly nonlinear perturbation expansion of the potential, which are proportional to the square of the wave amplitude.) Since the structural resonances of TLP’s occur above or below the frequency range of ocean-wave spectra, both the sum-frequency vertical loads and the difference-frequency horizontal loads are important. Considerable effort

is required to include all of the second-order hydrodynamic forcing effects since it is necessary to consider various quadratic interactions, including the inhomogeneous boundary condition which applies on the free surface. Several of the resulting second-order panel methods are described by Molin & Chen [11], Lee *et al.*, [12], Eatock Taylor and Chau, [13] and Lee & Newman [14]. Most of this work is based on the low-order panel method, because of its relative simplicity in implementation.

The need for better efficiency and accuracy, especially in second-order problems, motivated the development of higher-order methods where the geometry and solution are represented by polynomials or other basis functions. Eatock Taylor and Chau [13] and Liu *et al* [15] used isoparametric elements where the body surface and solution are represented by piecewise-continuous shape functions over each element. Okan and Umpleby [16] and Hsin *et al* [17] solved two-dimensional infinite-fluid problems using B-spline basis functions. B-splines are widely used for geometric modeling in computer-aided design (CAD) [18]. Thus it is possible to perform the hydrodynamic analysis directly from the geometric models created by CAD programs, without further approximation using piecewise higher-order elements. A more fundamental advantage of using B-splines is that their derivatives are continuous over the entire portion of the surface where the geometry is continuous. The B-spline method was developed for three-dimensional free-surface problems by Maniar [19], with further refinements and applications described by Lee *et al* [20].

A fundamental extension, first presented by Lee [21], retains the B-spline representation for the potential but permits the geometry to be described by any explicit expressions representing continuous surfaces. This provides great geometrical flexibility as the most convenient and suitable representation can be used to define the geometry. Newman and Lee [22] showed applications of this technique to several types of bodies represented exactly by mathematical formulae. Lee *et al* [23] integrated this methodology with the kernel of the CAD program MultiSurf, to provide a flexible and efficient analysis for various types of structures without the need to generate an intermediate geometry input file.

Typically, the computational effort of panel methods is proportional to $O(N^2)$ or $O(N^3)$. Here N is the number of unknowns. The Green function is evaluated $O(N^2)$ times to set up the linear system. Then the solution is evaluated either iteratively with $O(N^2)$ effort or by Gauss elimination with $O(N^3)$ effort. This effort may be reduced down to $O(N \log N)$ using acceleration algorithms such as the Fast Multipole Method (FMM) or the precorrected Fast Fourier Transform (pFFT). FMM is based on the use of

multipole expansion of the free surface Green function. The influence of the Green function is calculated by systematic application of Graf's addition theorem of Bessel functions following the hierarchical algorithm of Greengard & Rokhlin [24]. Application to the analysis of floating structures with up to 300,000 unknowns is made by Utsunomiya & Watanabe [25]. The method is expected to be less efficient for deep water due to slow convergence of multipole expansion of the Green function. The pFFT (precorrected Fast Fourier Transform) method was proposed for the integral equations with a general form of Green function by Phillips & White [26]. In the pFFT method, the influences of sources or dipoles distributed on the body surface, except in their vicinity, are approximated with sources (or dipoles) on a uniform grid surrounding the entire body or bodies. The influences of singularities on the nodes are evaluated by FFT with $O(N_g \log N_g)$ effort, where N_g is the number of nodes of the grid. Korsmeyer *et al* [27] applied the method to large complex offshore structures using up to 260000 unknowns. Both FMM and pFFT seek the solution iteratively and the methods may not be effective when the convergence is not sufficiently rapid.

In the following sections we provide more detailed descriptions of some of the developments above. Section 2 outlines the analytical formulation of the linear problem, including the boundary conditions, equations for the velocity potential and fluid velocity, and appropriate modifications of the integral equations that are used to remove irregular frequency effects and to analyze bodies with zero-thickness elements. In Section 3 we describe the numerical details associated with the low-order and higher-order panel methods. In Section 4 the pFFT method is briefly described and in Section 5 the second-order problem is reviewed. In Section 6 methods are described for the analysis of wave effects in the time domain. Section 7 includes a summary and conclusions.

A few computational examples are presented to show typical results and compare the different methods, based on the programs WAMIT [28] and TiMIT [29]. Many other examples can be studied from the demonstration program, documentation, and other publications which are available for download from the website www.wamit.com.

2 Formulation

The Cartesian coordinate system $\mathbf{x} = (x, y, z)$ is used with $z = 0$ the plane of the undisturbed free surface and $z < 0$ the fluid domain. It is assumed that the fluid is incompressible, inviscid, and the flow is irrotational. The fluid velocity is then represented at time t by the gradient of the velocity potential $\Phi(\mathbf{x}, t)$ satisfying the Laplace equation $\nabla^2 \Phi = 0$ in the fluid domain.

The fluid depth is either infinite, with vanishing motion at large depths, or constant with zero vertical velocity on the bottom boundary surface $z = -h$. One or more bodies are situated within the fluid domain, floating on the free surface or submerged. The portion of these bodies below the plane $z = 0$ is referred to collectively as the submerged surface S_b of the body or structure. This surface is assumed to be impermeable, with its normal velocity equal to the normal component of the fluid velocity. At large horizontal distances from the structure the wave field consists of a prescribed incident wave system plus outgoing waves associated with radiation and scattering. Surface tension is neglected.

2.1 The velocity potential and boundary conditions

Assuming small unsteady motions relative to the wavelength and relevant length scales of the body, the free-surface boundary condition can be linearized about $z = 0$. When the structure is not fixed, the body boundary condition is also linearized about its mean position. A time-harmonic dependence applies permitting the use of a complex notation for all oscillatory quantities. Thus the velocity potential is expressed by

$$\Phi(\mathbf{x}, t) = \text{Re}(\phi(\mathbf{x})e^{i\omega t}). \quad (1)$$

Here ω is the frequency of the regular incident wave in the linear analysis.

The real part of the product of all complex quantities with the factor $e^{i\omega t}$ is understood hereafter. The linearized form of the free-surface condition is

$$\phi_z - K\phi = 0 \quad (2)$$

on $z = 0$, where $K = \omega^2/g$ and g is the acceleration of gravity. Subscripts are used to denote partial differentiation with respect to the Cartesian coordinates (x, y, z) , normal vector n and time t . (Exceptions to this rule are the symbols $(n_x, dS_x, n_\xi, dS_\xi)$ which denote the normal vector or differential surface elements with respect to the \mathbf{x} or $\boldsymbol{\xi}$ coordinate systems, respectively.)

The linearization permits the decomposition of the velocity potential in the alternative forms

$$\phi = \phi_D + \phi_R = \phi_I + \phi_S + \phi_R. \quad (3)$$

Here ϕ_I is the potential of the incident wave, defined by

$$\phi_I = i\frac{gA}{\omega}Z(z)e^{-i\nu x \cos \beta - i\nu y \sin \beta}, \quad (4)$$

where A is the amplitude and β is the angle between the direction of propagation of the incident wave and the positive x -axis. For infinite water depth $Z(z) = e^{Kz}$ and $\nu = K$; for finite water depth h , $Z = \cosh[\nu(z+h)]/\cosh \nu h$ and the wavenumber ν is the positive real root of the dispersion relation $K = \nu \tanh \nu h$. Except for the incident-wave potential ϕ_I , all components of the potential satisfy the radiation condition of outgoing waves in the far field.

In (3) ϕ_S is the potential of the scattered field due to the presence of the bodies and subject to the boundary condition $\phi_{Sn} = -\phi_{In}$ on S_b . $\phi_D = \phi_I + \phi_S$ is the solution of the diffraction problem where $\phi_{Dn} = 0$ on S_b . (The definitions of the *scattered* and *diffraction* potentials are reversed in some references.)

The radiation potential ϕ_R represents the fluid disturbance due to the motions of the bodies and can be expressed in the form

$$\phi_R = i\omega \sum_j \xi_j \phi_j, \quad (5)$$

where ξ_j is the amplitude of motion in each degree of freedom considered. For a single rigid body with six degrees of freedom, $j = 1$ to 6 corresponding to surge, sway, heave, roll, pitch and yaw, respectively. The boundary condition on the body surface is then expressed in the form

$$\phi_{jn} = n_j, \quad (6)$$

where

$$(n_1, n_2, n_3) = \mathbf{n}, \quad (n_4, n_5, n_6) = \mathbf{x} \times \mathbf{n}. \quad (7)$$

Here \mathbf{n} and \mathbf{x} are the unit normal vector and position vector of points on the body surface. The convention adopted here is that \mathbf{n} points out of the fluid domain, and thus into the body. Body rotations and moments are referred to the origin $\mathbf{x} = 0$.

In the case of multiple bodies which are moving independently, it is straightforward to consider the additional degrees of freedom. For example, $j = 7, \dots, 12$ can be used to represent the same six degrees of freedom of the second body with

$$(n_7, n_8, n_9) = \mathbf{n}, \quad (n_{10}, n_{11}, n_{12}) = \mathbf{x} \times \mathbf{n} \quad (8)$$

applied on the second body, and with the convention that the components in (7) vanish on the second body while the components in (8) vanish on the first body.

In some cases it is useful to write the body boundary condition in the more general form

$$\phi_{jn} = \mathbf{u}_j(\mathbf{x}) \cdot \mathbf{n}(\mathbf{x}) \quad (9)$$

where $\mathbf{u}_j(\mathbf{x})$ is the displacement vector of the body boundary. The displacement vector can represent general mode shapes such as those corresponding to structural deflections, the motions of interior free surfaces inside moon-pools, or multiple bodies with constraints [30],[31].

2.2 Integral Equations

In the potential formulation Green's theorem is used to represent the velocity potential ϕ in the form

$$\left(\frac{2\pi}{4\pi}\right)\phi(\mathbf{x}) + \iint_{S_b} \phi G_{n\xi} dS_\xi = \iint_{S_b} \phi_n G dS_\xi. \quad (10)$$

Here the Green function $G(\mathbf{x}, \boldsymbol{\xi})$ corresponds physically to the potential of an oscillatory source, located at the point $\mathbf{x} = \boldsymbol{\xi}$ in the fluid domain and subject to the same boundary conditions on the free surface and bottom as ϕ , as well as the radiation condition. This Green function is well known, and various representations are useful [4, 32]. In (10) the factor 2π applies for points \mathbf{x} on S_b whereas the factor 4π applies for points \mathbf{x} in the interior domain of the fluid. The radiation potential ϕ_R and scattering potential ϕ_S can each be represented by (10). For the diffraction solution the more compact integral equation

$$\left(\frac{2\pi}{4\pi}\right)\phi_D(\mathbf{x}) + \iint_{S_b} \phi_D G_{n\xi} dS_\xi = 4\pi\phi_I(\mathbf{x}) \quad (11)$$

may be used. This has the advantage of a simpler right-hand side, and the incident wave is included in the solution, but in cases where the scattering effect of the body is relatively weak some accuracy may be lost due to the dominant role of the incident wave.

In the special case where \mathbf{x} is on S_b equations (10-11) give integral equations which can be solved for the unknown potentials on the body surface. After doing so, the same equations with the factor 4π can be used to evaluate the potential at field points within the fluid.

Alternatively, in the source formulation, the velocity potential is expressed by a source distribution or single-layer distribution, in the form

$$\phi(\mathbf{x}) = \iint_{S_b} \sigma G dS_\xi, \quad (12)$$

where the source strength σ is unknown. Evaluating the normal derivative on S_b leads to the integral equation for σ ,

$$\phi_n(\mathbf{x}) = 2\pi\sigma(\mathbf{x}) + \iint_{S_b} \sigma G_{n_x} dS_\xi, \quad (13)$$

where the left-hand side is evaluated from the body boundary condition.

Special attention is required to correctly interpret the dipole integrals in (10-11) and (13), involving G_{n_x} or G_{n_ξ} , when the point \mathbf{x} is on S_b . In this case a small area surrounding the singular point $\mathbf{x} = \boldsymbol{\xi}$ is excluded from the surface of integration, and the limit of the integral is evaluated as this area tends to zero. The same consideration applies to modified integral equations in Sections 2.5, 2.6 and 2.7 below. Further details are given in [2, 3, 4].

The relative advantages and disadvantages of the potential and source formulations are minor. Both involve the solutions of integral equations over the body surface with essentially the same level of computational effort. The potential formulation is more versatile, particularly in the representation of structures with relatively thin elements, but one disadvantage is that the evaluation of the fluid velocity requires second derivatives of the Green function.

2.3 Linearized pressure force on the body

The total pressure in the fluid is given by Bernoulli's equation

$$p = -\rho(\Phi_t + \nabla\Phi \cdot \nabla\Phi + gz). \quad (14)$$

The first term on the right side of (14) is the linear component of the dynamic pressure, which is written in the complex form as $-i\rho\omega\phi$. The second term is the quadratic pressure, which contributes to the second-order forces. The third term is the hydrostatic pressure, which contributes to the restoring forces.

The linearized hydrodynamic force (and moment) acting on the body are represented by the exciting-force coefficients

$$X_i = -i\omega\rho \iint_{S_b} \phi_D \phi_{in} dS, \quad (15)$$

due to the diffraction pressure field, and by the added-mass A_{ij} and damping B_{ij} coefficients

$$A_{ij} - (i/\omega)B_{ij} = \rho \iint_{S_b} \phi_j \phi_{in} dS, \quad (16)$$

due to the radiation field. Here the boundary condition (6) has been used and the index i corresponds to the component of the force (or moment), defined with the same convention as for the components of the radiation potential (5). For multiple bodies and generalized modes the definitions of the normal vector (8) and (9) carry over to the pressure force. The second index j in the added-mass and damping coefficients is associated with the corresponding mode of motion of the body.

The exciting-force coefficients can also be evaluated from the Haskind relations [2, 33]

$$X_i = -i\omega\rho \iint_{S_b} (\phi_{in}\phi_I - \phi_i\phi_{In}) dS. \quad (17)$$

2.4 Mean drift force on the body

The mean drift force (and moment) are important in many applications, particularly for bodies which are freely floating or restrained by relatively flexible moorings. The mean drift force is of second order in the wave amplitude, but it can be evaluated from the first-order linear potential [34]. Two alternatives are available including direct integration of the pressure on the body surface and the method which depends on momentum conservation. The pressure-integration method is more general, but it generally requires a more accurate solution to avoid local numerical errors. The momentum method is restricted to the horizontal components of the force and the vertical component of the moment, acting either on a single body by itself or on an ensemble of multiple bodies. In cases where both methods are applicable it is advisable to compare their results for consistency and convergence. It also is possible to use momentum conservation in the near field [35], which retains some of the advantages of both methods for multiple bodies, but this requires special programming and is not considered here.

For the pressure-integration method the contributions include the mean component of the pressure (14) from the time-average of the square of the fluid velocity, and products of the first-order pressure with the oscillatory variations of the body surface due to both the body motions and the runup at the waterline. The complete expression can be found in [28], Chapter 12 and [36].

In the momentum method the mean forces are expressed in terms of the Kochin functions

$$H(\theta) = \iint_{S_b} (\phi_{Bn}\phi_0 - \phi_B\phi_{0n}) dS, \quad (18)$$

where

$$\phi_0 = Z(z)e^{-i\nu x \cos \beta - i\nu y \sin \beta}$$

and $\phi_B = \phi_S + \phi_R$ is the part of the total potential due to the body. With this definition the drift force and moment are evaluated from the following expressions [37, 33]:

$$\begin{pmatrix} \bar{F}_x \\ \bar{F}_y \end{pmatrix} = \frac{\rho\nu^3}{8\pi K} \frac{c_p}{2c_g} \int_0^{2\pi} |H(\theta)|^2 \begin{pmatrix} \cos \theta \\ \sin \theta \end{pmatrix} d\theta - \frac{\rho\omega A\nu}{2K} \begin{pmatrix} \cos \beta \\ \sin \beta \end{pmatrix} \text{Im}H'(\pi + \beta) \quad (19)$$

$$\bar{M}_z = \frac{\rho\nu^2}{8\pi K} \frac{c_p}{2c_g} \text{Im} \int_0^{2\pi} H^*(\theta)H'(\theta) d\theta - \frac{\rho\omega A}{2K} \text{Re}H'(\beta). \quad (20)$$

Here c_p is the phase velocity, c_g is the group velocity, and the ratio

$$\frac{c_p}{2c_g} = \frac{Kh}{Kh + (\nu h)^2 - (Kh)^2}$$

is equal to one in the limit of infinite depth. In (20) H' denotes the derivative of the Kochin function with respect to its argument, and H^* denotes the complex conjugate.

The momentum method can be extended to the case where two incident waves are present with the same period and different heading angles [28].

2.5 Fluid velocity

Often it is necessary to evaluate the fluid velocity on the body surface, or at points within the fluid. An important application is in the evaluation of the mean drift force due to the quadratic pressure in (14). The quadratic pressure also specifies the boundary conditions in the second-order nonlinear problem which will be discussed subsequently.

For field points in the fluid it is straightforward to evaluate the gradients of the potential as given by (10-12), by interchanging the orders of differentiation and integration and replacing the Green function by its gradient. However special attention is required to evaluate the velocity on the body surface, due to the singularity of the Green function. The appropriate representations in this case are

$$2\pi\nabla\phi(\mathbf{x}) + \iint_{S_b} \phi\nabla G_{n_\xi} dS_\xi = \iint_{S_b} \phi_{n_\xi} \nabla G dS_\xi, \quad (21)$$

for the potential formulation derived from (10), and

$$\nabla\phi(\mathbf{x}) = 2\pi\sigma(\mathbf{x})\mathbf{n} + \iint_{S_b} \sigma\nabla G dS_\xi, \quad (22)$$

for the source formulation derived from (12).

Alternatively, for points on the body surface, the normal component of the velocity can be evaluated from the body boundary condition and the tangential components can be evaluated by differentiation of the solution for ϕ on this surface. This scheme is not suitable in the low-order method.

2.6 Elements of zero thickness

If the thickness of S_b tends toward zero the integral equations and their solutions are singular [38]. To overcome this difficulty a choice exists, either to increase the thickness artificially, or alternatively to modify the integral equations so that they apply to structures with elements of zero thickness. In the latter case, which is considered here, the appropriate representation of the potential is based on a distribution of dipoles only, also known as a double-layer distribution. The integral equation can be derived formally from the normal derivative of Green's equation. The resulting equation is analogous to the vortex distribution in lifting-surface problems [6].

The body surface is assumed to consist of two parts, a conventional portion S_b with nonzero thickness and another portion S_d of zero thickness, designated as the dipole surface. In this case the potential on S_b or in the interior of the fluid can be represented in the form

$$\left(\frac{2\pi}{4\pi}\right)\phi(\mathbf{x}) + \iint_{S_b} \phi G_{n_\xi} dS_\xi + \iint_{S_d} \Delta\phi G_{n_\xi} dS_\xi = \iint_{S_b} \phi_{n_\xi} G dS_\xi, \quad (23)$$

where $\Delta\phi$ is the difference of the potential on the two opposite sides of S_d . When \mathbf{x} is on the dipole surface S_d , the normal derivative of (23) can be used to derive the equation

$$\iint_{S_b} \phi G_{n_\xi n_x} dS_\xi + \iint_{S_d} \Delta\phi G_{n_\xi n_x} dS_\xi = -4\pi\phi_n(\mathbf{x}) + \iint_{S_b} \phi_{n_\xi} G_{n_x} dS_\xi. \quad (24)$$

An appropriate pair of coupled integral equations for this problem follow by using (23) for points on S_b and (24) for points on S_d to solve simultaneously for the unknowns ϕ on S_b and $\Delta\phi$ on S_d . In the diffraction problem the right-hand sides of these equations are replaced by $4\pi\phi_I(\mathbf{x})$ and $4\pi\phi_{In}(\mathbf{x})$.

2.7 Irregular frequencies

It is well known that the boundary-integral equations of wave problems involving the free-surface Green function either possess no solution or have a nonunique solution at a discrete set of *irregular frequencies*. For the potential and source formulations based on the integral equations above, the

irregular frequencies correspond to the eigenfrequencies of the homogeneous Dirichlet problem where the fluid and free surface are inside the body [39]. In the vicinity of these irregular frequencies numerical solutions of the integral equations are erroneous. Several numerical techniques have been developed to overcome this problem, by suppressing the occurrence of the corresponding eigenmodes.

The first technique, proposed by Ohmatsu [40], is based on imposing an extra boundary condition on the interior free surface, S_i . The Green's integral equation is then extended to include S_i where a homogeneous Neumann condition is imposed, with the result

$$\begin{aligned} 2\pi\phi(\mathbf{x}) + \iint_{S_b} \phi G_{n\xi} dS_\xi + \iint_{S_i} \phi G_{n\xi} dS_\xi &= \iint_{S_b} \phi_n G dS_\xi, \quad \mathbf{x} \in S_b, \\ -4\pi\phi(\mathbf{x}) + \iint_{S_b} \phi G_{n\xi} dS_\xi + \iint_{S_i} \phi G_{n\xi} dS_\xi &= \iint_{S_b} \phi_n G dS_\xi, \quad \mathbf{x} \in S_i. \end{aligned} \quad (25)$$

More detailed discussion and the extension to the source distribution is provided in [36] and [41]. This technique is widely used in free-surface problems.

The second technique, first applied in related work on acoustic scattering by Burton & Miller [42], is based on the idea that it is not possible to have nontrivial eigensolutions of the mixed homogeneous boundary condition $\phi + \alpha\phi_n = 0$ when the complex constant α has a nonzero imaginary part. The corresponding integral equation takes the form of a linear sum of Green's equation and its normal derivative

$$2\pi\phi(\mathbf{x}) + \iint_{S_b} \phi(G_{n\xi} + \alpha G_{n_x n_\xi}) dS_\xi = 2\pi\phi_n + \iint_{S_b} \phi_n(G + \alpha G_{n_x}) dS_\xi. \quad (26)$$

Results based on this technique with the low-order method are presented in [43]. However, experience has shown that the results based on this approach converge more slowly than those based on Ohmatsu's method.

The third technique [44, 45] is based on adding point singularities in the interior region to absorb the energy of the eigenmodes. This method is relatively simple to implement, but it fails in some cases unless special attention is given to the positions of the singularities.

3 Numerical procedures

The principal numerical tasks to be performed in the panel method include (1) representation of the geometry, (2) representation of the singularity distributions and velocity potential on the body surface, (3) numerical integration of the singularity distributions (influence functions), (4) solution of

the linear system, and (5) post-processing to evaluate the desired hydrodynamic parameters such as integrated forces or local pressures and velocities. Since most of these tasks are fundamentally different in the low-order and higher-order methods, they are discussed separately in the subsections below.

The procedures used to evaluate the free-surface Green functions, and to solve the linear system of equations, are the same for both methods. These are described briefly in the following paragraphs. Additional information can be found in [28], Chapter 12.

Free-surface Green functions, and their derivatives, are usually expressed as the sum of one or more Rankine singularities and a ‘regular’ component which is added to satisfy the free-surface boundary condition (2). The regular component includes a weakly-singular logarithmic term, which must be treated separately when the source point is on or close to the free surface. With this exception the regular component can be evaluated using polynomial approximations and eigenfunction expansions [7, 8]. An alternative scheme for the case of finite depth has been derived by Linton [46].

The linear system of equations which must be solved for the unknown singularity strengths, or for the coefficients of the B-splines in the higher-order method, is of the standard form with N equations and N unknowns. (Both are complex.) The conventional direct solver based on Gauss elimination is robust, but requires $O(N^3)$ computations. For problems where N is, say, greater than 1000, the iterative solver developed by Lee [9] is generally preferred to reduce the computational time. In some cases the convergence of the iterative solver is retarded due to ill-conditioning of the linear system. In the low-order method this is usually caused by hydrodynamic resonances, e.g. in the analysis of a structure with a moonpool. In the higher-order method, where the linear system is not diagonally-dominant, the direct solver is preferred unless N is large. A block iterative solver is useful in some situations, combining to some extent the efficiency of the iterative solver and the robustness of the direct solver.

The computational cost and memory allocation may be further reduced by employing acceleration methods such as pFFT and FMM, as described in the Introduction. The pFFT method is reviewed in Section 4.

3.1 Low-order method

The body surface is represented by a set of N quadrilateral panels. The geometry input file, which contains the vertex coordinates of each panel, should be prepared with a suitable pre-processor. A systematic set of two

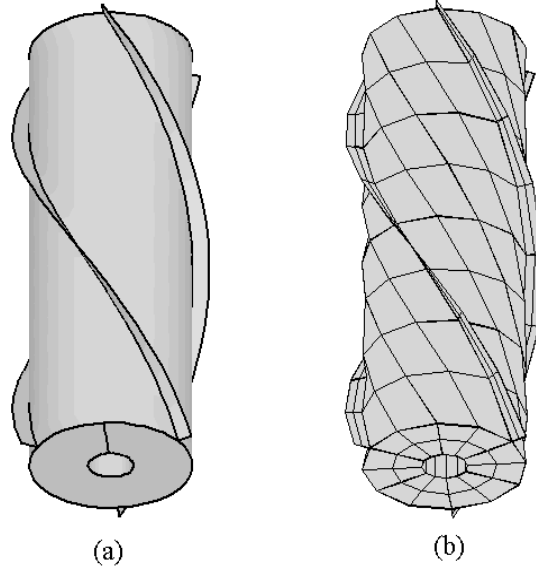


Figure 1: The submerged portion of a spar with three strakes and a concentric moonpool. The view is from below the structure, showing the bottom and the lower part of the moonpool wall. The exact structure is shown in the left figure (a). The principal dimensions are draft 100m, column radius 18m, moonpool radius 5m, and strake width 3.7m. The strakes are helical, and rotate through 180 degrees. The discretized structure used for the low-order method with $N = 264$ panels is shown in the right figure (b). The dark lines in (a) represent the edges of the patches used for the higher-order method, as described in Section 3.2.

or three input files should be used with increasing numbers of panels, to test for convergence. As the number of panels is increased and their size is decreased, the representation of the geometry should become increasingly accurate and similarly for the hydrodynamic outputs. The best way to confirm the accuracy of the results is to perform convergence tests in this manner, and to observe the differences in the outputs. Ideally the panel sides should be reduced by a factor of about two at each stage, implying a factor of 4 increase in N and a factor of (at least) 16 increase in the computing time. This rapid increase in computing time, and the labor required to prepare extra input files, tend to discourage the practice of testing for convergence.

As a specific example to illustrate the discussion, Figure 1(a) shows the submerged portion of a spar structure which consists of a cylindrical outer surface, a cylindrical inner moonpool, and three helical strakes. Figure 1(b) shows a relatively coarse discretization of this structure, represented by low-order panels with $N = 264$. Special attention has been given to ensuring that the sides of contiguous panels correspond along the edges where the strakes meet the cylinder outer surface, and where the outer and inner surfaces meet the bottom, so there are no ‘gaps’. In this example the panels are uniformly spaced. In applications where the local velocity near corners is important, as in the evaluation of the mean drift force by pressure integration, improved accuracy can be achieved by using nonuniform spacing with smaller panels near the corners of the bottom and outer edges of the strakes [47].

The integral equations (10-12) are evaluated by collocation, with \mathbf{x} equal to the coordinates of each panel centroid, to give a total of N equations. The integrals in (10-12) are carried out by summation over the corresponding integrals over each panel, where the values of the potential, normal velocity, or source strength are assumed constant. Thus the essential task is to evaluate the $N \times N$ matrices of influence functions, equal to the integral over the panel i of the Green function or its normal derivative, evaluated at the collocation point \mathbf{x}_j . For the regular part of the Green function these integrations are evaluated simply as the product of the panel area and the value of the integrand at the centroid. For the Rankine and logarithmic singularities the integrations are evaluated analytically when the singularity is nearby, and using multipole approximations when the collocation point is sufficiently far away from the panel. Suitable algorithms are derived in [48] and [49].

After solving for the values of the potential or source strength on each panel, the integrals required to evaluate the linear force coefficients (16-18) are carried out by summation over each panel. The potential or velocity at points in the fluid are evaluated from (10-12) or (21-22) using the same integration techniques as described in the preceding paragraph. The linearized pressure and wave elevation are simply proportional to the potential. The mean drift force and moment are evaluated in the pressure-integration method using (22) to evaluate the velocity components on the body and performing the surface integration in the same manner as above. For the momentum method the Kochin function (18) is integrated in the same manner. The azimuthal integrations in (19-20) can be performed with adaptive Gauss-Chebyshev quadratures, recursively doubling the number of

integration points until a specified tolerance is achieved.

3.2 Higher-order method

In the higher-order method, the integrals over the body surface and extended computational domains, such as the moonpool free surface, are carried out by numerical quadratures [28]. Thus the method describing the geometry is irrelevant to the solution procedure as long as the required geometric information is available at the points required for the numerical quadrature. In this way, the geometry can be described in the most convenient and accurate manner for a given body shape. The information required for this purpose includes the Cartesian coordinates, represented in terms of parametric coordinates as described below, and also the first partial derivatives of these transformations.

B-splines are used to provide a continuous representation of the solution, where this is appropriate. The order of the B-splines can be selected to ensure continuity of derivatives of the surface coordinates, i.e. the slope of this surface, as well as higher-order derivatives. However the body surface S_b may contain lines separating different continuous surfaces, as in the case of the spar shown in Figure 1(a) where there are lines of discontinuity along the outer and inner boundaries of the bottom and along the inner edges of the strakes.

In order to separate sub-surfaces which are discontinuous in this sense, we define each sub-surface by a separate ‘patch’. Eight patches are required for the spar in Figure 1(a), including three for the separate parts of the outer surface, three for the strakes, one for the bottom and one for the inner surface. The patch boundaries are outlined with dark lines in Figure 1(a).

A pair of parametric coordinates (u, v) are used to map the surface of each patch separately onto a square domain in parametric space. Thus the Cartesian coordinates of the points on each patch are defined by the mapping functions

$$x = X(u, v), \quad y = Y(u, v), \quad z = Z(u, v). \quad (27)$$

For example, the annular bottom of the spar, which covers the radial space $a < r < b$ and the azimuthal range $-\pi < \theta < \pi$, is mapped onto the square $-1 < u < 1$ and $-1 < v < 1$ by means of the transforms

$$r = a \frac{1-u}{2} + b \frac{1+u}{2}, \quad \theta = \pi v.$$

A cut is required along the radial line $\theta = \pi$ as shown in Figure 1(a).

On each patch the velocity potential is represented by a tensor product of B-spline basis functions

$$\phi(u, v) = \sum_{j=1}^{M_v} \sum_{i=1}^{M_u} \phi_{ij} U_i(u) V_j(v). \quad (28)$$

Here $U_i(u)$ and $V_j(v)$ are the B-spline basis functions of u and v , and M_u and M_v are the number of basis functions in u and v , respectively. The unknown coefficients ϕ_{ij} are determined by substituting this potential in the integral equation (10) or (11) and using a Galerkin procedure. More specifically, both sides of the integral equation are multiplied by the same set of basis functions, and integrated again over the boundary surface. The result is a linear system of equations for the coefficients ϕ_{ij} . The number of unknowns on each patch is $M_u \times M_v$ and the total number of unknowns is the sum of this product over all patches.

The accuracy of the representation (28) depends on the order of the basis functions and the numbers of these functions M_u and M_v . Generally we use basis functions of order three (quadratic) or four (cubic). These ensure continuity of the first or second derivative, corresponding to the tangential velocity or its gradient on the body surface, respectively. In order to control the number of basis functions we extend the geometric notion of panels by subdividing the parametric domain of each patch into $N_u \times N_v$ panels. It is important to note that, while these panels correspond to rectangles in the parametric space, they conform exactly to the body surface as defined by the mapping functions (27). Thus the physical manifestation of each panel is not restricted to be flat or rectangular.

The number of basis functions and the number of panels are related by

$$M_u = N_u + K_u - 1, \quad M_v = N_v + K_v - 1, \quad (29)$$

where K_u and K_v are the orders of the B-splines. Further information regarding the B-spline basis functions can be found in [18]. In standard B-spline terminology, the subdividing points between panels correspond to knots. Important advantages of the higher-order method are that the geometry can be defined exactly, or with whatever precision is deemed appropriate, separately from the solution for the velocity potential. The accuracy of the solution is then controlled simply by increasing the number of panels. This greatly facilitates the performance of convergence tests.

All of the required integrations in the higher-order method are performed using Gauss quadratures in parametric space. These include the *inner* integrations in the integral equations (10) or (11), the *outer* integra-

tions used in the Galerkin procedure, and ultimately the surface integrations required for post-processing to evaluate the hydrodynamic force coefficients, Kochin functions, or the potential and velocity at points in the fluid. Special algorithms are used to remove the Rankine and logarithmic singularities in the Green functions, when required. Further details are given in [28].

3.3 Computational example

In order to provide an illustration of the relative efficiency and accuracy of the low-order and higher-order methods, we shall consider the diffraction problem for the spar buoy shown in Figure 1(a). In both methods the thickness of the strakes is ignored and they are modeled as zero-thickness elements. The analysis is then made by applying the coupled integral equations (23) and (24). Later, the same geometry is used to illustrate a method for evaluating the wave elevation inside the moonpool using generalized modes.

The integral equation is solved with three different discretizations in both the low- and higher-order methods, to examine the convergence of the computational results. In the low-order method, the numbers of panels N are 264, 1056 and 4224 and the dimension of the linear system is the same. The first of these three representations is shown in Figure 1(b). The solution of the linear system is obtained iteratively, which is more efficient than the Gauss elimination for large N . The computing times per frequency for the diffraction solution with one wave direction are 0.2, 3 and 60 seconds, respectively, in ascending order of N , on a PC with a 1 GHz Pentium processor. For additional wave directions, or radiation solutions, the computing time would increase somewhat, due to the need for separate iteration for the solution of the linear system for each of these solutions.

In the higher-order method 46, 184 and 736 subdivisions are used. Third-order B-spline basis functions are used on all patches. The corresponding numbers of unknowns N are 162, 384 and 1104. The resulting linear system is solved directly using Gauss elimination. The iterative method is not effective for the linear system resulting from the Galerkin approach, which is adopted in the higher-order method. However since the dimension of the linear system is relatively small in the higher-order method, the use of the direct method is not a practical problem. The computing times per frequency for one wave direction are 0.5, 7, 115 seconds, respectively. The additional time required is negligible for the diffraction solutions at other wave directions, or for the radiation solutions, since these are obtained by back substitutions.

Figure 2 shows comparisons of the surge exciting force and yaw moment based on the two methods, for a range of wave periods. For this structure the

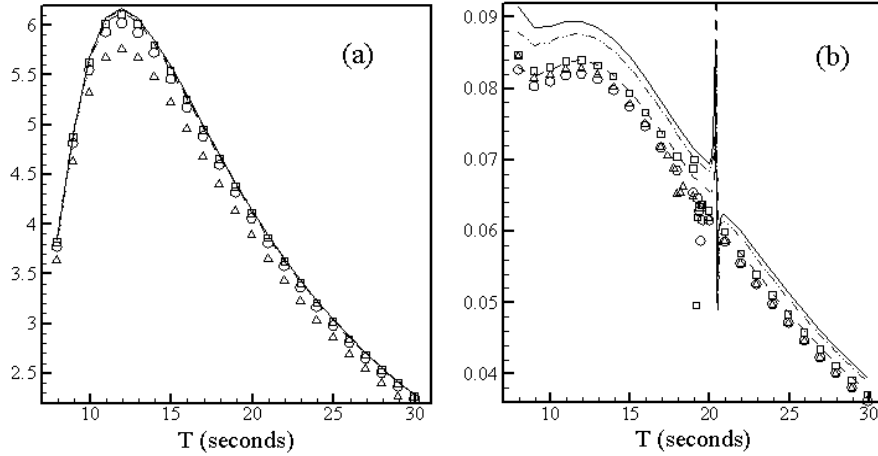


Figure 2: The surge force (a) and yaw moment (b) on the spar. The force is normalized by $\rho g A L^2$ and the moment by $\rho g A L^3$ where ρ is the water density, g the gravitational constant, A the incident wave amplitude and L is the radius of the spar. The lines represent the higher-order method and the symbols represent the low-order method. Dashed, dash-dot and solid lines correspond to $N = 162, 384$ and 1104 , respectively. Triangles, circles and squares correspond to $N = 414, 1656$ and 6264 .

yaw moment is due entirely to the pressure difference across the opposite sides of the strakes. Thus the yaw moment is relatively small. For both modes, the results based on the higher-order method are more accurate and rapidly convergent. This can be seen more clearly in Figure 3, which shows the absolute errors at the period of 12 seconds where the surge force peaks. Here the error is defined as the difference based on the higher-order method using 3648 unknowns.

The irregularity of the yaw moment near 20 seconds is due to the pumping-mode resonance in the moonpool. The resonant period can be estimated from the formula $T = 2\pi\sqrt{D/g} = 20.0$, where D is the draft (cf. [3], equation 3.87). The actual resonance occurs at 20.4 seconds. In a narrow moonpool such as this, the sloshing resonances occur at high frequencies and are of less practical concern. The pumping mode is highly tuned, as shown in Figure 4, with the peak of the computed elevation at the center of the

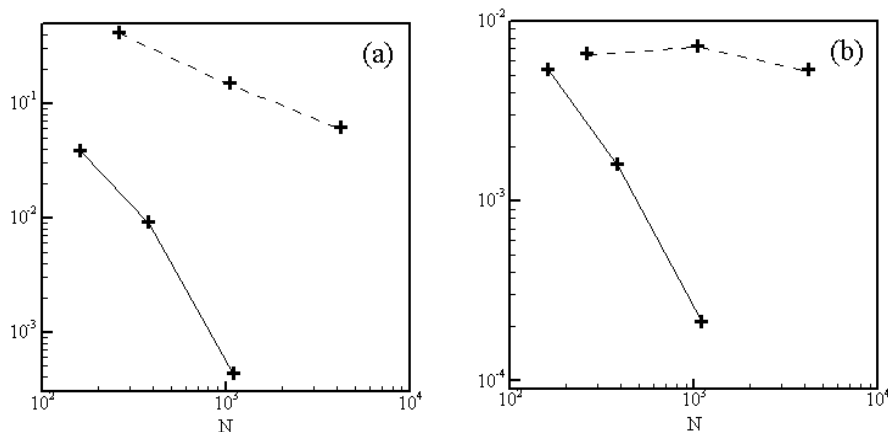


Figure 3: Absolute errors in the surge force (a) and yaw moment (b), plotted vs. the number of unknowns for the period 12 seconds. The solid line is the result from the higher-order method and the dashed line from the low-order method. Other definitions are the same as those in Figure 2

moonpool 76 times the incident-wave amplitude. Thus it is important to correct for the damping effects associated with separation near the bottom corners of the moonpool and other sources of viscous drag.

A semi-empirical damping correction can be included by using generalized modes to represent the free-surface motion of the moonpool, as described in [28], Appendix A17. For this purpose a radiation solution ϕ_7 is included as a generalized mode to represent the pumping mode. The appropriate boundary condition (9) is with $\mathbf{u}_7 = (0, 0, 1)$ on the free surface inside the moonpool and $\mathbf{u}_7 = (0, 0, 0)$ on S_b . Thus the computational domain is extended to include the free surface in the moonpool. The generalized mode is included in the equations of motion, with zero mass and gravitational restoring forces imposed but with a constant coefficient of external damping. After the solution is obtained, the response amplitude ξ_7 represents the average amplitude of the free surface elevation inside the moonpool. Additional modes can be included to represent sloshing modes in the moonpool, but this is not necessary in the present example.

The validity of this technique is confirmed by Figure 4a, which com-

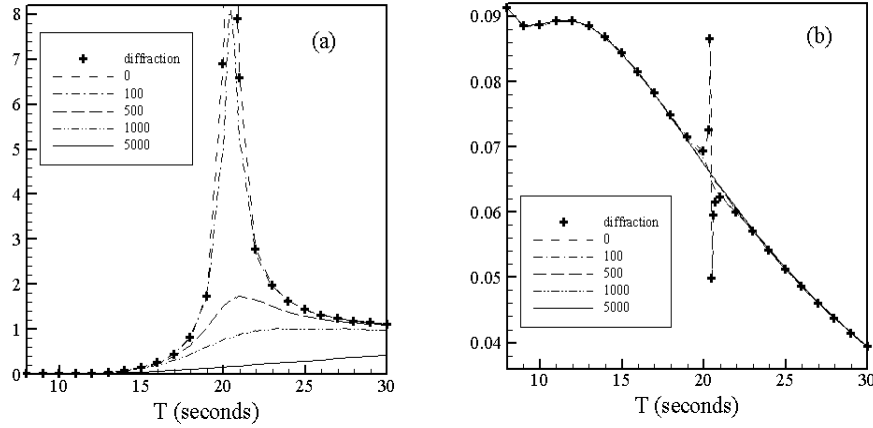


Figure 4: Amplitude of the free surface elevation at the center of the moonpool, normalized by the incident wave amplitude (a), and the yaw moment (b). The symbol (+) denotes the results obtained from the diffraction solution. Lines denote the results using a generalized mode for the pumping mode. Numbers are the linearized damping coefficient in N/(m/s).

compares the free-surface elevation at the center of the moonpool obtained from (10), using the diffraction solution with a conventional free-surface boundary condition imposed in the moonpool, and the amplitude of the generalized mode ξ_7 computed without external damping. Also shown are results with various values of the damping coefficient applied to the pumping mode. A relatively small damping force suppresses the large elevation due to the resonance in the pumping mode. The wave elevation approaches the incident wave amplitude inside the moonpool for long waves. Further reduction of the elevation below the incident waves requires a significantly larger damping force, as may be expected. Figure 4b shows the same comparison for the yaw moment, confirming that the irregularity noted in Figure 2 is also removed by the moonpool damping.

4 The pFFT method

The traditional approach for the solution of the integral equations in the low-order method is described in the preceding sections. The influence

matrices of the discrete linear system are dense and the iterative method of solution requires $O(N^2)$ effort where N is the number of panels. To make the iteration efficient, $O(N^2)$ memory allocation is necessary to store all elements of the matrices. As an example, in the solution of the potential formulation, we evaluate the influence matrix due to normal dipoles, D , and its product with the solution $D\phi$. Separating the influence from the nearby dipoles, D_n , and that from the far field, D_f , the above product may be evaluated separately by $D_n\phi$ and $D_f\phi$. D_n is sparse and its evaluation, storage, and product with ϕ are all $O(N)$. $D_f\phi$ can be evaluated by the pFFT method without explicit evaluation of D_f .

It is convenient to consider the procedure of pFFT in three steps, namely the projection, convolution and interpolation following Phillips & White [26]. The procedure can be summarized in the form

$$D_f\phi = I(\mathbf{x}, \mathbf{x}_g)C(\mathbf{x}_g; \boldsymbol{\xi}_g)P(\boldsymbol{\xi}_g, \boldsymbol{\xi})\phi(\boldsymbol{\xi}) \quad (30)$$

where \mathbf{x}_g and $\boldsymbol{\xi}_g$ are the coordinates of the nodes of a uniform grid surrounding the entire body and P , C and I denote the matrices representing each of three steps. $\phi = \phi(\boldsymbol{\xi})$ is the unknown velocity potential.

The projection calculates the strength of point wave sources on the nearby nodes of each panel such that the influence from the point sources is equivalent to the influence of the panel at the far field. The projection matrix P is $N_g \times N$ where N_g is the number of grid nodes. It is a sparse matrix, however, because only nearby nodes of each panel are considered. Each column vector of P , denoted by $P_j(\boldsymbol{\xi}_g)$, represents the projection of each panel. This may be evaluated from

$$\iint_{\text{panel}_j} G_{n\xi}(\mathbf{x}; \boldsymbol{\xi})dS_\xi = \sum G(\mathbf{x}; \boldsymbol{\xi}_g)P_j^T(\boldsymbol{\xi}_g) \quad (31)$$

using appropriate control points at the far field in place of \mathbf{x} . The summation is over the nearby grid nodes.

After the projection is completed, the wave sources on the body surface are replaced by point sources on the grid nodes with the source strength $\phi_g = P\phi$. The influence of each source at the other nodes can be evaluated by three-dimensional convolution. The influences between the nodes in the near field, including the self-influence, are not relevant and arbitrary values may be assigned to them. The influence of the wave source is decomposed into two components, one from $G_T(x - \xi, y - \eta, z - \zeta)$ and the other from $G_H(x - \xi, y - \eta, z + \zeta)$. On a uniform grid G_T leads to a triply-nested Toeplitz matrix and G_H to a doubly-nested Toeplitz matrix in x and y and a Hankel matrix in z . From these matrices, it is straightforward to construct

two circulant matrices with periodic elements as shown in [26]. Finally, the products of the circulant matrices and ϕ_g can be evaluated efficiently from the relation $C\phi_g = F^{-1}[F(C_1)F(\phi_g)]$ where C_1 denotes the first row of the circulant matrices and F and F^{-1} denote the discrete Fourier transform and the inverse Fourier transform, respectively [50]. The computational effort for the convolution is $O(N_g \log N_g)$ and the memory allocation is $O(N_g)$.

The interpolation calculates the potentials at the collocation points from those at nearby nodes. The interpolation matrix I is $N \times N_g$ and each row represents the interpolation for each collocation point. I is sparse with nonzero elements only for the nearby nodes of the collocation points. The row vectors, $I_i(\xi_g)$, may be obtained in a similar manner for P_j from

$$G(\mathbf{x}; \xi_i) = \sum G(\mathbf{x}; \xi_g) I_i(\xi_g) \quad (32)$$

using appropriate control points at the far field in place of \mathbf{x} .

The pFFT method is reviewed here in conjunction with the low-order method. While the Galerkin approach adopted in the higher-order method produces a more compact form, it leads to a linear system which is not diagonally-dominant, and thus it may be unsuitable for the iterative solution method. As suggested in [19], this is because 2π , arising from the self-influence, is distributed to the off-diagonal terms spanned by the B-spline basis function in the Galerkin approach.

number of cylinders	number of unknowns	time per iteration
20 by 5	9600	0.2
36 by 9	31104	0.8
60 by 15	86400	3.4
100 by 25	240000	7.6

Table 1: The size of the linear system and the computational time required for one iteration, based on pFFT method. The CPU time is measured in seconds on a PC with a 1GHz Pentium processor.

In order to illustrate the computing time based on the pFFT method, arrays consisting of multiple cylinders of identical shape are considered. This type of structure may also be analyzed by the method described in [53]. The radius of the individual cylinder is 11.5m and the draft is 20m. The spacing between the adjacent cylinders is 40m. Each cylinder is represented by 96 panels. Four different arrays are considered as shown in Table 1. The largest array, which spans an area of 4km by 1km, is typical of some

structures which have been considered for floating airports. Table 1 shows the number of unknowns and corresponding computational time required for each iteration based on the pFFT method.

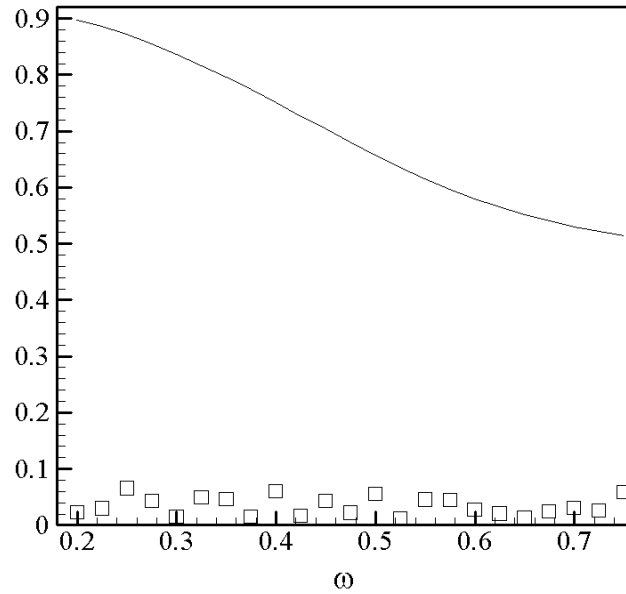


Figure 5: Mean drift force in the transverse direction on a large array of cylinders (square symbols) and a barge (line). Both structures occupy a horizontal area 4km long by 1km wide, and have the same displaced volume. The wave direction is at 45 degrees from the sides. The drift forces are normalized by $\rho g A^2 L$ where ρ is the water density, g the gravitational constant, A the incident wave amplitude and $L = 2km$.

The required number of iterations and thus the computing time for the solution of the linear system varies significantly depending on the period of the incident waves. For example, when $N=240000$, the number of iterations required to reach the average of the element of the residual vector equal to $1.E-4$ gradually increases from 16 for the wave period 31.4 seconds to 400 for 8.33 seconds. The required memory is about 1Gb when $N=240000$, and

increases linearly with N .

In Figure 5, a comparison is made of the mean drift force on the largest array in Table 1 and on a barge with the same horizontal dimensions, 4km by 1km, and with the same volume as the array. Thus the draft of the barge is 5m. The barge is discretized with 43000 panels and analyzed by the pFFT method as well. The wave direction is 45 degree from the longitudinal direction. The mean drift forces are evaluated by the momentum method described in Section 2.4. The comparison shows that the mean drift force on the array of cylinders is an order of magnitude smaller than on the barge.

5 The second-order problem

The second-order potential, which results from quadratic interactions between the first-order quantities with frequencies ω_i and ω_j , is given by

$$\Phi^{(2)}(\mathbf{x}, t) = \text{Re}\{\phi^+(\mathbf{x})e^{i\Omega^+ t} + \phi^-(\mathbf{x})e^{i\Omega^- t}\}, \quad (33)$$

where an explicit distinction is made between the sum (+) and difference (−) frequency-components with the respective frequencies $\Omega^\pm = \omega_i \pm \omega_j$. These may be further decomposed in the form

$$\phi^\pm = \phi_I^\pm + \phi_S^\pm + i\Omega^\pm \sum_k \xi_k^\pm \phi_k^\pm. \quad (34)$$

Here ξ_k^\pm is the second-order component of the motion amplitude. The radiation potential ϕ_k^\pm is subject to the same conditions as the radiation potential in the linear problem described in Section 2, but with the frequency Ω^\pm substituted in the free-surface condition (2). ϕ_I^\pm and ϕ_S^\pm will be referred to as the second-order incident-wave and scattering potentials. These potentials are subject to inhomogeneous free-surface conditions, with the forcing equal to

$$q_f^\pm = \frac{i}{4}\omega_i\phi_i(\phi_{jzz}^{(*)} - K_j\phi_{jz}^{(*)}) \pm \frac{i}{4}\omega_j\phi_j^{(*)}(\phi_{izz} - K_i\phi_{iz}) - \frac{i}{2}\Omega^\pm \nabla\phi_i \cdot \nabla\phi_j^{(*)}. \quad (35)$$

Here $K_{i,j} = \omega_{i,j}^2/g$ and $\phi_j^{(*)}$ denotes either ϕ_j or its complex conjugate for q_f^+ or q_f^- , respectively. This forcing can be further decomposed in the form, $q_f^\pm = q_I^\pm + q_S^\pm$. q_I^\pm represents the forcing due to the interaction of two linear incident waves only in (35) and is defined over the entire free surface. q_S^\pm is the rest of the forcing which includes the quadratic interactions between the incident and the body disturbance waves, $\phi_B = \phi_S + \phi_R$ and also the quadratic terms associated with ϕ_B alone.

The second-order incident-wave potential, ϕ_I^\pm , subject to the forcing q_I^\pm on $z = 0$, is given in the form

$$\phi_I^\pm = \frac{q_I^\pm(x, y)Z(k^\pm z)}{-\Omega^\pm + gk^\pm \tanh k^\pm h} \quad (36)$$

where $k^\pm = \sqrt{\nu_i^2 + \nu_j^2 \pm 2\nu_i\nu_j \cos(\beta_i - \beta_j)}$. In the case of infinite water depth, when $\beta_i = \beta_j$, q_I^\pm and ϕ_I^\pm both vanish.

The second-order scattering potential, ϕ_S^\pm , is subject to the free-surface condition $-\Omega^\pm \phi_S^\pm + g\phi_{S,z}^\pm = q_S^\pm$ on $z = 0$ and the body boundary condition $\phi_{S,n}^\pm = q_b^\pm$ on S_b . The body forcing q_b^\pm is equal to $-\phi_{I,n}^\pm$ for fixed bodies. If the bodies oscillate, q_b^\pm is complicated due to the first-order body motions. The complete expression of q_b^\pm , in this case, can be found in [34] and in the equations (3.11) and (3.12) of [36].

Green's theorem is applied to the Green function of the linear problem and ϕ_S^\pm to give a representation for the latter in the form

$$\left(\frac{2\pi}{4\pi}\right)\phi_S^\pm(\mathbf{x}) + \iint_{S_b} \phi_S^\pm G_{n_\xi} dS_\xi = \iint_{S_b} q_b^\pm G dS_\xi + \iint_{S_f} (q_s^\pm/g) G dS_\xi \quad (37)$$

where S_f denotes the free surface exterior to the bodies. The closure integral in the far field vanishes due to the radiation condition of ϕ_S^\pm [51].

After the solution of (37) is obtained, the force on the body can be evaluated in the form

$$F_p^\pm = -i\rho\Omega^\pm \iint_{S_b} (\phi_I^\pm + \phi_S^\pm)\phi_{k,n}^\pm dS \quad (38)$$

where ϕ_k^\pm is the radiation potential in equation (34). Alternatively, in the 'indirect' approach introduced by Molin [51] and Lighthill [52], the force can be evaluated without explicit solution of ϕ_S^\pm from

$$F_p^\pm = -i\rho\Omega^\pm \left[\iint_{S_b} (\phi_k^\pm \phi_{S,n}^\pm + \phi_I^\pm \phi_{k,n}^\pm) dS + \iint_{S_f} (q_s^\pm/g)\phi_k^\pm dS \right]. \quad (39)$$

In this context ϕ_k^\pm is also known as the 'assisting potential'.

In (37) and (39) the evaluation of the integrals over the infinite extent of the free surface S_f is a major computational burden. To evaluate these integrals efficiently, the free surface is divided in two parts, separated by a 'partition' circle. This circle should be sufficiently large so that the evanescent terms are negligibly small in the region outside. These evanescent modes tend to zero in proportion to the factors $e^{-r/h}$ in finite water

depth and $(Kr)^{-3}$ in infinite depth, where r is the radial coordinate. In general, the computational effort increases with the water depth.

In the region outside the partition circle the wave source, the first order potentials and the assisting potential are expanded in Fourier-Bessel series. After integrating the trigonometric functions with respect to the angular coordinate, the integrals are reduced to sums of one-dimensional integrals of triple products of Hankel and Bessel functions in the radial coordinate. The latter integrals are nontrivial, but they can be evaluated numerically with appropriate algorithms which are described in detail in the Appendix B of [36]. Inside the partition circle direct numerical quadratures are used. When the partition circle is large, it is useful to introduce a smaller concentric circle separating the inner region close to the bodies and an annular region between the two circles. In the inner region the free surface is subdivided using panels and the integration is carried out in a piecewise manner by numerical quadratures. In the annular region the Gauss-Chebyshev and Gauss-Legendre quadratures are used with respect to the angular- and radial-coordinates, respectively, as discussed in [28].

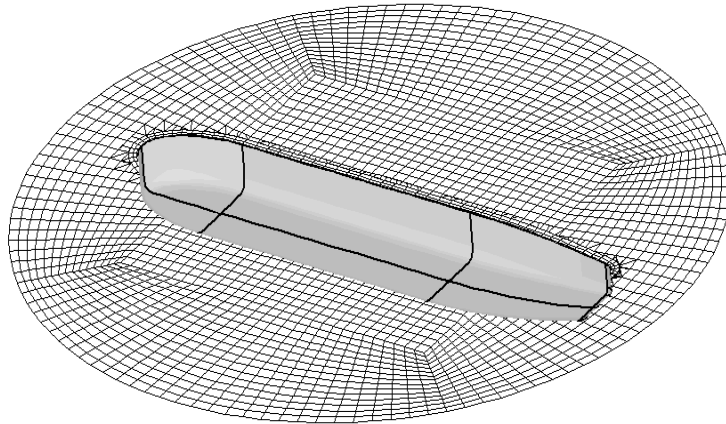


Figure 6: Fish-eye view of FPSO and the free surface discretization on the inner region.

In addition to the second-order velocity potential, the quadratic pressure acting on the mean body surface due to the interactions of the first order quantities contribute to the second-order force. This force is defined

as the quadratic force F_q^\pm . When two linear frequencies are the same, F_q^- is equal to the mean drift force discussed in Section 2. The complete expressions for F_q^\pm can be found in [36].

The sum-frequency velocity potential decays slowly in depth and is the dominant cause of high-frequency vertical forces on structures such as TLPs. It is also important for the prediction of the free surface elevation near structures. Applications of panel methods to various problems where the sum-frequency solution is important are discussed in [11] - [15]. On the other hand, in the prediction of the slowly-varying horizontal forces, the difference-frequency velocity potential is often ignored because the mean drift force provides a reasonable approximation when the difference frequency is small. In light of recent interest in FPSO's where the control of the slowly varying motion is important, the difference-frequency force on a generic form of FPSO is calculated for a range of difference frequencies to illustrate the relative importance of the complete difference frequency forces in this case.

The FPSO used for this example is shown in Figure 6, together with the discretization of the inner free surface. The ship's length is 300m, the beam 50m and the draft 25m. The higher-order method is used for this analysis, with the shape of the FPSO defined analytically using seven patches on one side of the body. Three patches describe the bow, midship and stern, respectively, and one patch is on the transom. Three patches are used to connect the stern to the transom preserving geometric continuity. Thus the velocity potential and the fluid velocity on the body surface are continuous except on the vertical line at the bow. Except in the vicinity of this line, the tangential fluid velocity on the body surface can be evaluated from the analytic derivative of the B-spline basis function. On the free surface inside a circle of radius 200m, the integration of the quadratic forcing is made using flat panels as shown in Figure 6. The intermediate annular region extends outward 100m to the partition circle of radius 300m.

Figure 7(a) shows the second-order difference-frequency sway force on the FPSO in a beam sea. Five values of the difference frequency are included, with $\delta\omega = 0, 0.05, 0.1, 0.15$ and 0.2 radians. The force corresponding to $\delta\omega = 0$ is the mean drift force. The separate components of the second-order difference frequency force are plotted in Figures 7(b-d). Figure 7(b) shows the magnitude of the quadratic force F_q . It is interesting to observe that F_q is close to the mean drift force for the higher frequencies where the first-order pressure acting on the oscillatory variations of the body surface due to the runup at the waterline is dominant. On the other hand, F_q is significantly different from the mean force for the lower frequen-

cies where the quadratic product of the fluid velocity is important as well. Figure 7(c) shows that the component due to the second-order incident and scattering waves increases more rapidly as the average frequency increases for larger $\delta\omega$. The component due to the free-surface forcing, which is shown in Figure 7(d), does not increase as rapidly but still contributes significantly when $\delta\omega$ is large.

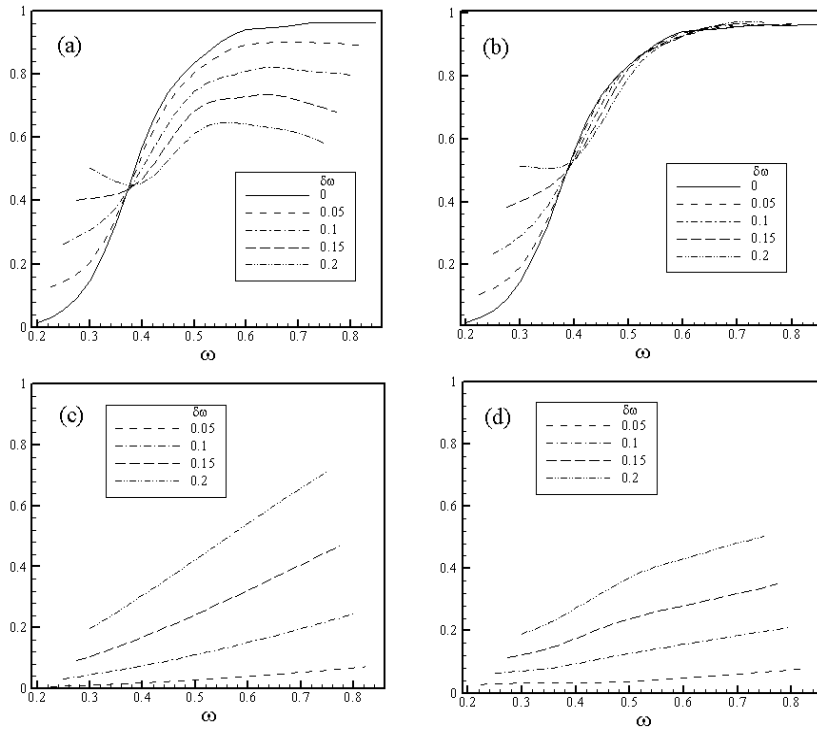


Figure 7: Second-order difference-frequency sway force on the FPSO. $\delta\omega$ is the difference of the two linear wave frequencies and ω is their average. (a) shows the total force. The quadratic force F_q is shown in (b). (c) shows the force component due to the incident wave and its scattering due to the presence of the body. (d) shows the component due to the quadratic forcing on the free surface. The sum of the last two components is F_p .

For these computations third-order B-splines are used to represent both the first- and second-order solutions, with 69 patch subdivisions. The total

number of unknowns is 175. On the free surface, one half of the inner region is discretized with 1426 panels. On the intermediate region, 6th order Gauss-Chebyshev and 10th order Gauss-Legendre quadratures are used. The computational results are converged within 1% compared to the results from finer discretization. The computational time for the complete second-order solution for each difference frequency is about 1 minute on a PC with a 1 GHz Pentium processor.

For bodies with sharp corners, such as a vertical truncated cylinder, the tangential fluid velocity is unbounded at the corners. The quadratic forces evaluated from the product of fluid velocities and the product of fluid velocity and the body motion are significantly less accurate than the linear forces. The accuracy of the second-order forces are also affected similarly. Nonuniform geometric mapping near the corners improves the accuracy somewhat, as discussed in [22] and [23].

6 Time-domain impulse-response functions

Some applications require solutions in the time domain, instead of the more common analysis in the frequency domain. Important examples include the coupled analysis of linear hydrodynamic loads with nonlinear structural response or with nonlinear viscous forces. For such problems the hydrodynamic loads can be described in the time domain by impulse-response functions (IRF's), which correspond physically to the response of the body, as a function of time t , to canonical impulsive disturbances at $t = 0$.

For the radiation forces, corresponding to the added-mass and damping coefficients (16), it is customary to define the IRF $L_{ij}(t)$ as the i -th component of the force acting on the body in response to impulsive motion in mode j , in otherwise calm water. Different types of impulsive motion can be defined, as discussed in [29]. It is assumed here that the acceleration of the body is a delta-function $\delta(t)$, and the velocity is a unit-step-function $H(t)$ increasing from zero to one at $t = 0$. In an analogous manner we define an impulsive incident wave, moving in a specified direction β , such that the wave elevation at the origin $\mathbf{x} = 0$ is equal to $\delta(t)$; for $t < 0$ there are no waves ahead of the origin, and *vice versa*.

As in other fields of linear systems theory, physically relevant incident wave systems and body motions can be constructed from these canonical IRF's by superposition. Simulations and solutions of the time-domain equations of motion can be computed by time-convolutions of the IRF's and body motions. Moreover, the IRF's can be related to the corresponding force coefficients in the frequency domain by Fourier transformation. This permits the use of outputs from frequency-domain panel programs for time-domain

analyses. A technique for performing this transformation is described here.

For the radiation forces, the fundamental relations between the time- and frequency-domain express the added-mass coefficient A_{ij} and damping coefficient B_{ij} in terms of Fourier transforms of the IRF $L_{ij}(t)$ by the following relations [29, 37]

$$A_{ij}(\omega) - A_{ij}(\infty) = \int_0^\infty L_{ij}(t) \cos \omega t dt, \quad (40)$$

$$B_{ij}(\omega) = \omega \int_0^\infty L_{ij}(t) \sin \omega t dt. \quad (41)$$

The inverse-transforms of (40-41) give alternative relations for the IRF:

$$L_{ij}(t) = \frac{2}{\pi} \int_0^\infty [A_{ij}(\omega) - A_{ij}(\infty)] \cos \omega t d\omega, \quad (42)$$

$$L_{ij}(t) = \frac{2}{\pi} \int_0^\infty \frac{B_{ij}(\omega)}{\omega} \sin \omega t d\omega. \quad (43)$$

Fundamental properties of the IRF's for the radiation forces are that these functions are real, and from the principle of causality they must vanish for $t < 0$.

Similar relations exist for the exciting forces (15) and (17), where we define the corresponding IRF's by $K_i(t)$. These functions are real, but unlike the radiation IRF's they are nonzero for $t < 0$ since the incident-wave system is present for both negative and positive times. With the appropriate physical ranges ($0 \leq \omega < \infty$) and ($-\infty < t < \infty$), the complex Fourier transforms are as follows:

$$X_i(\omega) = \int_{-\infty}^\infty K_i(t) e^{-i\omega t} dt, \quad (44)$$

$$2\pi K_i(t) = \int_{-\infty}^\infty X_i(\omega) e^{i\omega t} d\omega. \quad (45)$$

Since K_i is real, $X_i(-\omega) = X_i^*(\omega)$, and thus

$$2\pi K_i(t) = \int_0^\infty [X_i(\omega) e^{i\omega t} + X_i^*(\omega) e^{-i\omega t}] d\omega, \quad (46)$$

or

$$K_i(t) = \frac{1}{\pi} \int_0^\infty [\operatorname{Re}(X_i) \cos \omega t - \operatorname{Im}(X_i) \sin \omega t] d\omega. \quad (47)$$

The principal computational task required to obtain the IRF's is to evaluate (42) or (43), and (47). For this purpose the frequency-domain

coefficients should be evaluated at a large number of uniformly-spaced frequencies ω_n . Here $n = 0, 1, 2, \dots, N$, $\omega_0 = 0$, and $\omega_{n+1} - \omega_n = \Delta$ is constant. This permits the use of Filon quadratures to perform the numerical integration in an accurate and efficient manner for all physically relevant values of time (cf. [54], equation 25.4.47).

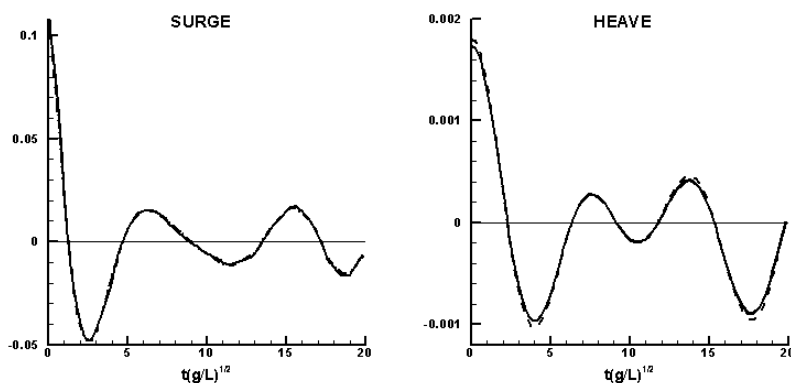


Figure 8: Surge and heave impulse-response functions $L'(t)$ for the ISSC TLP. The solid and dashed/dot lines are derived from computations in the frequency domain using the alternative transforms (42) and (43). The dashed lines are from the low-order time-domain program TiMIT. These results are normalized by the factor $\rho g L^2$ where $L = 43.125\text{m}$ is the half-spacing between adjacent columns.

Special considerations must be given to the limits $\omega = 0$ and $\omega = \infty$. Since the damping coefficient vanishes in both of these limits, it is generally preferable to use (43) instead of (42). On the other hand it is useful to compare these two complementary integrals, and thus worth some effort to evaluate (42). In general the added mass is nonzero in both limits. These can be evaluated as special cases where the free-surface condition (2) is replaced by homogeneous Neumann ($\phi_z = 0$) and Dirichlet ($\phi = 0$) conditions, respectively, with solutions following from the method of images. With respect to (47), the exciting forces are effectively hydrostatic in the limit $\omega = 0$, and can be evaluated directly or by extrapolation from adjacent small nonzero frequencies. When $\omega = \infty$ the exciting forces vanish.

In view of these considerations it is appropriate to truncate the semi-

infinite range of integration in (43) and (47) at a sufficiently large frequency $\Omega = \omega_N = N\Delta$, testing that N is sufficiently large and that Δ is sufficiently small by performing convergence tests. A similar procedure is used for (42), but with the addition of a truncation correction. For this purpose an asymptotic approximation for the added mass at high frequencies can be derived by partial integration of (40):

$$A_{ij}(\omega) - A_{ij}(\infty) = -\frac{1}{\omega} \int_0^\infty L'_{ij}(t) \sin \omega t dt \simeq -L'(0)\omega^{-2}. \quad (48)$$

Here the neglected integral is of order ω^{-3} .

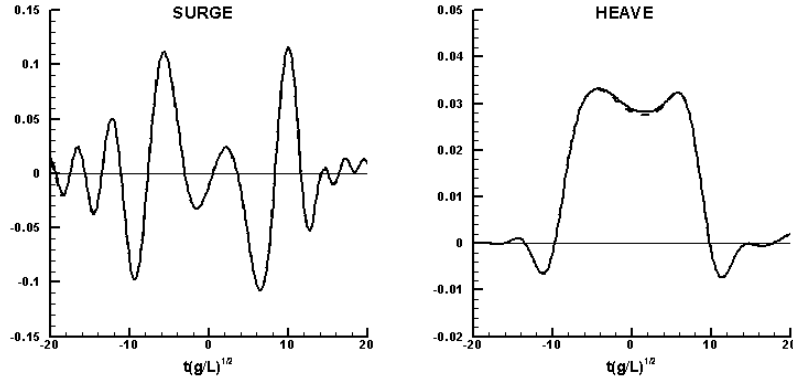


Figure 9: Surge and heave exciting-force impulse-response functions $K(t)$ for the ISSC TLP. The solid lines are derived from computations in the frequency-domain using (47). The dashed lines are from the low-order time-domain program TiMIT. These results are normalized by the factor $\rho(gL)^{3/2}$ where $L = 43.125\text{m}$ is the half-spacing between adjacent columns.

The truncation correction for (42) is defined by

$$\Lambda_{ij}(t) = \frac{2}{\pi} \int_{\Omega}^{\infty} [A_{ij}(\omega) - A_{ij}(\infty)] \cos \omega t d\omega. \quad (49)$$

This can be approximated, using (48), if Ω is sufficiently large:

$$\Lambda_{ij}(t) \simeq -\frac{2}{\pi} L'_{ij}(0) \int_{\Omega}^{\infty} \omega^{-2} \cos \omega t d\omega = -\frac{2}{\pi\Omega} L'_{ij}(0) [\cos \Omega t + \Omega t \text{si}(\Omega t)]. \quad (50)$$

Here we follow the notation of [54] (equation 5.2.26) for the sine integral

$$\int_z^\infty \frac{\sin t}{t} dt = -\text{si}(z).$$

The constant $L'_{ij}(0)$ can be evaluated by differentiating (43), with the result

$$L'_{ij}(0) = \frac{2}{\pi} \int_0^\infty B_{ij}(\omega) d\omega \simeq \frac{2}{\pi} \int_0^\Omega B_{ij}(\omega) d\omega. \quad (51)$$

Thus

$$\Lambda_{ij}(t) \simeq -\frac{4}{\pi^2 \Omega} [\cos \Omega t + \Omega t \text{si}(\Omega t)] \int_0^\Omega B_{ij}(\omega) d\omega. \quad (52)$$

Results are shown in Figures 8 and 9 for the ISSC TLP. Figure 8 shows the time-derivatives of the radiation IRF's for surge and pitch, and Figure 9 shows the exciting forces. The frequency-domain computations were performed using the higher-order method, with exact representation of the geometry as explained in [28], Appendix A14. A total of 101 frequencies were used, with $\Delta = 0.05$ radians/second. The other inputs are the same as in [28], Appendix A14, with the exception that the parameters used to specify the number of basis functions on each patch were doubled. (This resulted in a total of 384 unknowns in the linear system.) In Figure 8 separate curves are plotted based on (42) and (43) above; these are practically indistinguishable within graphical precision. Also shown in Figures 8 and 9 are computations performed directly in the time domain using the low-order program TiMIT [29] with 1012 panels on one quadrant and the same number of unknowns. (This panelization and the geometry of the body are described in [28], Appendices A6 and A7.) The effects of wave interaction between the columns are significant, and these result in IRF's with noticeable oscillatory features. Thus the comparisons shown in Figures 8 and 9 are considered to be representative of relatively complex applications. (The derivative $L'(t)$ is plotted in Figure 8 to facilitate comparison with the results from TiMIT, where the body velocity rather than the acceleration is equal to $\delta(t)$. The derivatives of (42) and (43) shown in Figure 8 are evaluated numerically, by first-order finite differences using a time-step of 0.2 seconds.)

7 Summary and Conclusions

This Chapter describes the development of panel methods applied to the first- and second-order analysis of wave interaction with stationary bodies.

The relevant boundary-value problems and the integral-equation formulations are reviewed. Detailed discussion on the solution procedure is provided to contrast the low-order and higher-order panel methods. The pFFT acceleration method is also discussed, reflecting recent interest in very large offshore structures. Also presented is a numerical technique to transform frequency-domain results into impulse-response functions suitable for use in time-domain simulations.

The higher-order panel method described here makes use of B-splines to represent the velocity potential. Naturally the pressure and the fluid velocity are continuous on each patch and can be evaluated at any point. This is particularly useful for interfacing with structural analysis programs where the pressure is required at a large set of prescribed points on the body surface. Continuity of the solution is also highly advantageous in cases where the pressure and velocity fields are required over a dense mesh as inputs to a Navier-Stokes solver, to account for localized viscous effects.

A distinctive feature of the higher-order method presented here is that the solution procedure is completely independent from how the geometry is prescribed. Thus the method can be applied to any geometric model made with continuously-defined surfaces. This provides great flexibility for a broad range of applications, since the geometry can be described in the most convenient and accurate manner among various options.

In most applications the higher-order method also gives more rapid convergence of the results, compared to the low-order method, so that it is simpler to achieve a high degree of accuracy. As illustrated in the computation of the spar with strakes, significantly more accurate results can be obtained from the higher-order method and it requires less computational time to achieve comparable accuracy of the solution. The application to the FPSO shows that the second-order forces on practical structures can be evaluated with substantial accuracy as well.

The accelerated pFFT method is restricted at present to use with the low-order method. Nevertheless it can be very advantageous for the analysis of very large structures such as those proposed for floating airports and mobile offshore bases. It is shown that the iteration can be carried out substantially faster by the pFFT method in comparison with conventional matrix-vector multiplication. The method also requires an order of magnitude less memory, which is linearly proportional to the number of unknowns. It is observed however the iteration converges slowly as the number of unknowns increases. It is desirable to improve the rate of convergence, for example, by developing appropriate preconditioners.

The impulse-response functions in the time domain are evaluated by

Fourier transformation of the frequency-domain results. It is noted that the zero- and infinite-frequency limits must be considered when they are nontrivial. Since a wide frequency range is required in the transform, it is important to remove the effect of the irregular frequencies which occur in the relatively high frequency range.

The computational time may be reduced significantly by exploiting the geometric symmetry of structures, when this exists. For structures like TLPs which have two planes of symmetry the computational domain may be reduced to one quadrant by decomposing the solution into four components, each symmetric or antisymmetric with respect to the planes of symmetry. Thus the number of independent solutions is increased by a factor of 4 but the number of unknowns is reduced by 1/4. The computational time for the procedures requiring $O(N^2)$ and $O(N^3)$ operations can be reduced by 1/4 and 1/16, respectively, compared to a solution which does not exploit symmetry. For structures such as ship hulls which have one plane of symmetry the corresponding reduction factors are 1/2 and 1/4. The spar shown in Figure 1 has no planes of symmetry, due to the helical strakes, and the analysis of this structure must be carried out in the full three-dimensional domain. There is no computational saving associated with planes of symmetry for the pFFT method since that procedure only requires $O(N)$ operations.

Panel methods are now indispensable tools for the prediction of wave effects on large offshore structures. These methods have become more powerful and versatile due to the various developments reviewed in this chapter. The linear and second-order nonlinear analysis for three-dimensional structures and the interactions among them are performed routinely. As illustrated in the computational examples, the analysis can be made accurately and efficiently on current personal computers.

References

- [1] Lamb, H. *Hydrodynamics, 6th Edition*. Cambridge University Press: Cambridge, UK, 1932 and Dover: New York, 1945.
- [2] Newman, J. N. *Marine Hydrodynamics*, MIT Press: Cambridge, USA, 1977.
- [3] Faltinsen, O. M. *Sea loads on ships and offshore structures*, Cambridge University Press: Cambridge, UK, 1991.
- [4] Linton, C. M. and McIver, P. *Handbook of Mathematical Techniques for Wave/Structure Interactions*, Chapman & Hall/CRC: 2001.

- [5] Hess, J. and Smith, A.M.O. Calculation of nonlifting potential flow about arbitrary three-dimensional bodies. *J. Ship Research*, **8**, pp. 22-44, 1994.
- [6] Hess, J. Panel methods in computational fluid dynamics. *Ann. Rev. Fluid Mech.*, **22**, pp. 255-274, 1990.
- [7] Newman, J. N. Algorithms for the Free-Surface Green Function. *J. Engineering Mathematics*, **19**, pp. 57-67, 1985.
- [8] Newman, J. N. The approximation of free-surface Green functions. *Retirement Meeting for Professor F.J. Ursell* Manchester, UK, March 1990. Published in *Wave Asymptotics*, eds. P.A. Martin and G.R. Wickham, 107-135, Cambridge University Press: Cambridge, UK 1992.
- [9] Lee, C.-H. *Numerical Methods For Boundary Integral Equations in Wave Body Interactions*, Ph.D. Thesis, Dept. of Ocean Engineering, MIT, 1988.
- [10] Korsmeyer, F. T., Lee, C.-H., Newman, J. N., and Scлавounos, P. D. The analysis of wave interactions with tension leg platforms. *Proceedings Seventh Int'l. Conf. on Offshore Mech. and Arctic Engineering*, eds. J.S. Chung, S.K. Chakrabarti, ASME: New York, pp. 1-14 1988.
- [11] Molin, B. and Chen, X. P. *Vertical resonant motions of tension leg platforms*. Institut Français du Pétrole, 1990.
- [12] Lee C.-H., Newman, J.N., Kim, M.H., and Yue, D.K.P. The computation of second-order wave loads. *Proceedings Tenth Int'l. Conf. on Offshore Mech. and Arctic Engineering*, eds. S.K. Chakrabarti, H. Maeda, G.E. Hearn, A.N. Williams, ASME: New York, pp. 113-124, 1991.
- [13] Eatock Taylor, R. & Chau, F. P. Wave diffraction theory – some developments in linear and nonlinear theory. *Journal of Offshore Mechanics and Arctic Engineering*, **114**, pp. 185-194, 1992.
- [14] Lee, C.-H. and Newman, J. N. Second-order wave effects on offshore structures. *Proceedings of BOSS '94*, ed. C. Chryssostomidis, Pergamon, **2**, pp. 133-146, 1994.
- [15] Liu, Y.H., Kim, M.H. and Kim C.H. The Computation of Second-Order Mean and Double-Frequency Wave Loads on a Compliant TLP by HOBEM, *International Journal of Offshore and Polar Engineering*, **5(2)**, pp. 111-119, 1995.

- [16] Okan M.B. and Umpleby S.M. The Use of B-splines for the Calculation of Two-dimensional Potential Flow Around Arbitrary Bodies. *International Shipbuilding Progress*, **32(370)**, pp. 151-155, 1985.
- [17] Hsin, C.-Y., Kerwin, J. E. & Newman, J. N. A higher-order panel method based on B-splines. *Proceedings of Sixth International Conference on Numerical Ship Hydrodynamics*, eds. V.C. Patel and F. Stern, National Academy Press: Washington, pp. 133-151, 1993.
- [18] Rogers D.F. and Adams J.A. *Mathematical Elements for Computer Graphics*, McGraw-Hill: New York, 1990.
- [19] Maniar, H. *A three dimensional higher order panel method based on B-splines.*, Ph.D. thesis, Dept. of Ocean Engineering, MIT, 1995.
- [20] Lee, C.-H., Maniar, H.D., Newman, J.N., and Zhu, X. Computations of wave loads using a B-spline panel method. *Proceedings of 21st Symposium on Naval Hydrodynamics*, National Academy Press: Washington, pp. 75-92, 1996.
- [21] Lee, C.-H. Wave interaction with huge floating structure. *Proceedings of BOSS '97*, Delft, ed J.H. Vugts, pp. 253-268, 1997.
- [22] Newman, J.N. and Lee, C.-H. Boundary-Element Methods in Offshore Structure Analysis. *Proceedings of 20th Int'l Conference on Offshore Mech. and Arctic Engineering*, ASME: New York, 2001; *Journal of Offshore Mechanics and Arctic Engineering*, **124**, pp. 81-89, 2002.
- [23] Lee, C.-H., Letcher, J.S. Jr., Mack, R.G. II, Newman, J.N., Shook, D.M. and Stanley, E. Integration of Geometry Definition and Wave Analysis Software. *Proceedings of twenty-first Int'l Conference on Offshore Mech. and Arctic Engineering*, ASME: New York, 2002.
- [24] Greengard L. and Rokhlin V. A Fast Algorithm for Particle Simulations. *Journal of Computational Physics*, **73**, pp. 325-348, 1987.
- [25] Utsunomiya T. and Watanabe E. Accelerated Higher Order Boundary Element Method for Wave Diffraction/Radiation Problems and Its Applications, *Proceedings of Twelfth International Offshore and Polar Engineering Conference*, eds. J.S Chung, M. Sayed, M. Kashiwagi, T. Setoguchi, and S.W. Hong, ISOPE: Cupertino, pp. 305-312, 2002.
- [26] Phillips, J. R. and White, J.K. A precorrected-FFT Method for electrostatic analysis of complicated 3-D structures. *IEEE Trans. on Computer-Aided Design*, **16(10)**, pp. 1059-1072, 1997.

- [27] Korsmeyer, F.T. Klemas, T.J., White, J.K and Phillips, J.R. Fast Hydrodynamic Analysis of Large Offshore Structures. *Proceedings of Ninth Int'l Offshore and Polar Engineering Conf.*, ISOPE: Brest, pp. 27-34, 1999.
- [28] Wamit, Inc. *WAMIT User Manual, Version 6.1*, WAMIT Inc.: Chestnut Hill, 2002. (Available for download from the website www.wamit.com)
- [29] Korsmeyer, F. T., Bingham, H. B. & Newman, J. N. *TiMIT – a panel-method for transient wave-body interactions*. Research Laboratory of Electronics, MIT, 1999.
- [30] Newman, J. N. Wave effects on deformable bodies. *Applied Ocean Research*, **16**(1), pp. 47-59, 1994.
- [31] Newman, J.N. Wave Effects on Multiple Bodies. *Hydrodynamics in Ship and Ocean Engineering*, ed. M. Kashiwagi, RIAM, Kyushu University: Kyushu, pp. 1-24, 2001.
- [32] Wehausen, J.V. and Laitone, E.V. Surface Waves. *Handbuch der Physik*, **9**, pp. 446-778, 1960. (Available for download from the website www.coe.berkeley.edu/SurfaceWaves)
- [33] Mei, C. C. *The applied dynamics of ocean surface waves*, Wiley: New York 1983; World Scientific Pub Co; 2nd edition 1989.
- [34] Ogilvie, T. F. Second-order hydrodynamic effects on ocean platforms. *Proc. Intl. Workshop on Ship and Platform Motions*, ed. R. W. Yeung, University of California, Berkeley, pp. 205-265, 1983.
- [35] Ferreira, M. D., and Lee, C.-H. Computation of second-order mean wave forces and moments in multibody interaction, *Proceedings of BOSS '94*, ed. C. Chryssostomidis, Pergamon, **2**, pp. 303-313, 1994.
- [36] Lee, C.-H. *WAMIT Theory Manual*, MIT Report 95-2, Dept. of Ocean Engineering, MIT, 1995.
- [37] Wehausen, J. V. The motion of floating bodies. *Ann. Rev. of Fluid Mechanics* **3**, pp. 237-268, 1971.
- [38] Martin, P.A. and Rizzo F.J. Boundary Integral Equations for Bodies of Small, but Finite, Thickness. *Proceedings of Eighth Int'l Workshop on Water Waves and Floating Bodies*, ed. J. Pawlowski, National Research

- Council Canada: St. John's, pp. 91-94, 1993. (Available for download from the website www.rina.org.uk)
- [39] John, F. On the motion of floating bodies, II. *Comm. Pure and Applied Mathematics*, **3**, pp. 45-101, 1950.
- [40] Ohmatsu, S. On the Irregular Frequencies in the Theory of Oscillating Bodies in a Free Surface. *Papers of Ship Research Institute*, **48**, pp. 1-13, 1975.
- [41] Zhu, X. *Irregular frequency removal from the boundary integral equation for the wave-body problem*, MSc Thesis, Dept. of Ocean Engineering, MIT, 1994.
- [42] Burton, A.J. and Miller, G.F. The Application of Integral Equation Methods to the Numerical Solution of Some Exterior Boundary-Value Problems. *Proc. Roy. Soc.*, **A323**, pp. 201-220, 1971.
- [43] Lee, C.-H. and Sclavounos, P.D. Removing the Irregular Frequencies from Integral Equations in Wave-Body Interactions. *J. Fluid Mech.*, **207**, pp. 393-418, 1989.
- [44] Ogilvie, T.F. and Shin, Y.S. Integral equation solution for time-dependent free surface problems. *J. Soc. Nav. Arch. Japan*, **143**, pp. 86-96, 1977.
- [45] Ursell, F. Irregular frequencies and the motion of floating bodies. *J. Fluid Mech.*, **105**, pp. 143-165, 1981.
- [46] Linton, C. M. Rapidly convergent representations for Green's functions for Laplace's equation. *Proc. Roy. Soc. Lond., A* **455**, pp. 1767-1797, 1999.
- [47] Lee, C.-H. and Newman, J. N. Sensitivity of wave loads to the discretization of bodies. *Proceedings of BOSS '92*, eds. M. H. Patel & R. Gibbins, BPP Technical Services Ltd: London, **1**, pp. 50-64, 1992.
- [48] Newman, J. N. Distribution of Sources and Dipoles over a Quadrilateral. *Journal of Engineering Mathematics*, **20**, pp. 113-126, 1986.
- [49] Newman, J. N. and Sclavounos, P. D. The Computation of Wave Loads on Large Offshore Structures. *Proceedings of BOSS '88*, eds. T. Moan, N. Janbu & O. Faltinsen, Tapir: Trondheim, **2**, pp. 605-622, 1988.

- [50] Strang, G. *Introduction to Applied Mathematics*, Wellesley-Cambridge Press: Wellesley, 1986.
- [51] Molin, B. Second Order Diffraction Loads upon Three Dimensional Bodies. *Applied Ocean Research*, **1**, pp. 197-202, 1979.
- [52] Lighthill, M.J. Waves and Hydrodynamic Loading. *Proc. of 2nd Int. Conf. on the Behaviour of Offshore Structure (BOSS '79)*, eds. H.S. Stephens & S.M. Knight, BHRA Fluid Engineering, Cranfield, **1**, pp. 1-40, 1979.
- [53] Chakrabarti, S. Multibody interaction - Hybrid method *Numerical Models in Fluid-Structure Interaction*, ed. S. Chakrabarti, WIT Press: Southampton, 2003.
- [54] Abramowitz, M. & Stegun, I. A. *Handbook of mathematical functions with formulas, graphs, and mathematical tables*. U.S. Government Printing Office: Washington and Dover: New York, 1964.